Journal of Applied Fluid Mechanics, Vol. 10, No. 1, pp. 283-291, 2017.
Available online at www.jafmonline.net, ISSN 1735-3572, EISSN 1735-3645.
DOI: 10.18869/acadpub.jafm.73.238.26335

Effect of Geometry Modifications on the Vectoring Performance of a Controlled Jet

M. N. Tomac

Department of Mechanical Engineering, Abdullah Gul University, Kayseri, 38080, Turkey

Email: mehmet.tomac@agu.edu.tr

(Received March 25, 2016; accepted June 7, 2016)

ABSTRACT

Jet vectoring performances of ten different designs with various depths and geometrical outlines were quantified through constant temperature anemometry measurements for a Reynolds number range from 10,000 to 30,000 by using passive and active flow control methods at cold flow. The reference design was based on NASA's double throat nozzle concept and a self-injection double throat nozzle design that uses similar flow control concept as the reference design, were also tested for performance comparison. Furthermore, jet vectoring performance of a single throat design, utilizing Coanda effect for jet vectoring, was also quantified. Results indicated jet vectoring angles starting from 2° up to 47° for a control jet flow rate range from 1% up to 10% with respect to the primary jet flow rate in the investigated Re range. Maximum jet vectoring angle was achieved with a single throat design which incorporates small step geometry before the Coanda surface for more effective flow attachment and these results were compared with the vectoring performance of the double throat nozzle designs.

Keywords: Jet vectoring; Active flow control; Constant temperature anemometry.

1. INTRODUCTION

Jet flows are the most common type of flow and used as the main source of propulsion in many engineering applications and also in nature (e.g., jet engines, rockets, cephalopods). Jets have higher momentum compared to the surrounding medium and this momentum is dominantly concentrated in one direction which is generally in the opposite direction of the motion of the object. The direction of this motion is strictly related to the angle that the jet is issued at. Altering this angle by means of jet vectoring methods particularly for thrust vectoring purposes has been subject to many studies and mainly classified as mechanical and fluidic vectoring concepts (Bougas and Hornung 2013).

Mechanical methods may include rotating and/or extending nozzles, vanes, post-exit flaps or vanes, aft-hoods, deflected divergent flaps, and rotation of the entire system (Berrier and Mason 1988; Berrier and Taylor 1990; Carson and Capone 1991). Although vectoring angles as high as 90° can be achieved by mechanical methods, there are a number of disadvantages that come along with these methods such as increased weight and space requirement due to additional mechanical components, design, manufacturing and maintenance complexity, longer system reaction time, and increased radar cross section.

Fluidic flow control methods offer variety of advantages mainly due to no moving part design of the actuators and the simplicity of the overall vectoring control system. Performances of variety of fluidic vectoring concepts such as throat shifting, shock-vector, and counterflow with various flow control actuation were investigated for decades (Strykowski *et al.* 1996; Flamm 1998; Deere 2000; Deere 2003; Deere *et al.* 2003; Deere *et al.* 2005; Dores *et al.* 2006; Bettridge *et al.* 2006; Benard *et al.* 2007; Wilde *et al.* 2008; Allen and Smith 2009). Various actuators and approaches also have been used for jet vectoring such as blowing and suction (Pack and Seifert 2001, Smith and Glezer 2002, Guo *et al.* 2003), plasma actuators (Porter *et al.* 2009, Matsuno *et al.* 2012), injection jets (Raman *et al.* 2005) including injection of a liquid phase fluid as control jet (Heidari and Pouramir 2016).

Fluidic control methods (FCM) are needed to be chosen specific to the nozzle design and flow regime. However, all these FCM are based on either injection or suction from a control port with

significantly lower flow rate compared to the main jet flow rate. Due to this injection or suction vectoring can be obtained by changing the character of the shock (the normal shock can be skewed to an oblique shock which changes the main jet flow direction), shifting the throat to a new aerodynamic location (shifting or skewing of the sonic plane), or attaching the main jet to a preferred nozzle wall due to Coanda effect.

To address wide range of conditions double throat nozzle (DTN) concept was developed by NASA Langley Research Center (Deere *et al.* 2003; Deere *et al.* 2005). DTN design is basically a nozzle consisting of two identical throats in which the control fluid is injected from the first throat to make the jet attach to the opposite inner wall of the nozzle's recessed cavity due to separation and the vectored jet leaves the nozzle from the second throat.

Figure 1 shows the Mach contours obtained through the preliminary numerical analyses which were done in the early phase of this study for no control and 2% fluidic injection cases on a DTN design based on the dimensions given in a study by Bougas and Hornung (2013). In this figure, injection location and the separated region can clearly be seen while the primary jet is vectored 8° relative to the x-axis.

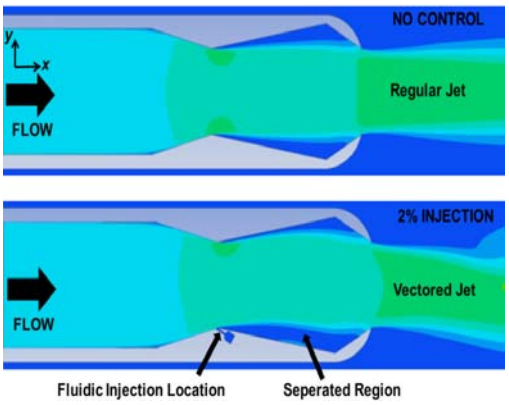

Fig. 1. Sample CFD results representing the DTN geometry and the working mechanism with no control (top), and 2% injection cases (bottom).

In this study, vectoring performances of ten designs with various depths and geometrical outlines were extracted through constant temperature anemometry (CTA) measurements for Reynolds number (Re) range from 10,000 to 30,000 where Re was calculated based on this hydraulic diameter of the exit, D_h. Results indicated that the self-injection designs exhibited lower performance compared to DTN designs and increased depth generally reduces the vectoring angle. Furthermore, a single-throat design with a step geometry (Reba 1966; Yang *et al.* 2007) for increased attachment of the jets to Coanda (Coanda 1936) surfaces performed the best among all the designs tested in this work and observed to be a promising design for future studies.

2. EXPERIMENTAL SETUP

2.1 Experimental Models

The DTN designs that were used in this work were scaled versions of the design provided in a study by Bougas and Hornung (2013), as shown in Fig. 2 with the letter codes (A, B, C etc.), adopted to provide major dimensions for all experimental models. In here, the fluidic injector on the first throat is shown with light color arrow while the letters from A to D represent the dimensions and the letters E to H represent the angles.

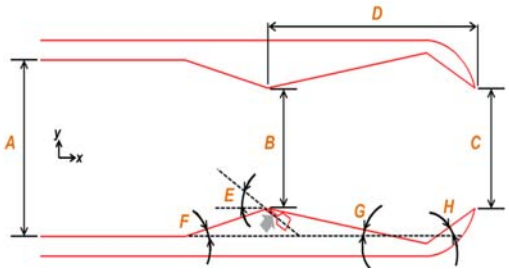

Fig. 2. DTN geometry and dimensional letter codes.

Tables 1 and 2 show the dimensional details of the experimental models considered in this study. In the Table 1, dimensions for A to D, depth (α), and D_h are given in millimeters and angles are (E-H) given in degrees in Table 2. Also there is no H angle value (shown with -) for Model 10 (M10) since it comprised of a single throat. Following this table the geometrical outlines of the ten experimental models are provided in Fig. 3. In here, the Coanda surface used in M10 was designed as a straight line with angle of 50° with respect to exit centerline. Also note that the jet vectoring models 2, 4, 6, and 8 are passively controlled (no external blowing or energy input) and the rest of the models are actively controlled.

Table 1 Main dimensions of the models in mm

	A	*B*	*C*	*D*	α	D_h
M1	39.6	26	26	58	3	5.38
M2	39.6	26	26	58	3	5.38
M3	39.6	26	26	58	5.6	9.22
M4	39.6	26	26	58	5.6	9.22
M5	39.6	26	26	58	9	13.37
M6	39.6	26	26	58	9	13.37
M7	19.8	13	13	29	3	4.88
M8	19.8	13	13	29	3	4.88
M9	19.8	13	13	29	3	4.88
M10	19.8	13	28	8	3	5.42

Table 2 Main angles of the models in degrees

	E	*F*	*G*	*H*
M1	30	15	10	30
M2	30	15	10	30
M3	30	15	10	30
M4	30	15	10	30
M5	30	15	10	30
M6	30	15	10	30
M7	30	15	10	30
M8	45	15	10	30
M9	45	15	10	45
M10	90	15	48	-

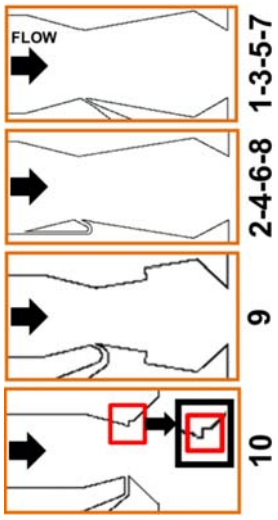

Fig. 3. Geometrical outlines of the experimental models.

The experimental models were manufactured from clear acrylic by laser cutting. Each model consists of a base part, a middle part, and a top part as shown in Fig. 4. All these parts were combined by acrylic glue and tested for leaks. The bottom right image in the Fig. 4 shows how these parts were attached to each other and the flow paths of the primary and control jets.

2.2 Experimental Setup and Methodology

Velocity profiles which were determined through the constant temperature anemometry (CTA) were used in order to obtain the vectoring performance of a model. The experimental setup used for the measurements is shown in Fig. 5. The pressurized air to this setup was provided by PUMA PDN60-2M silent 60 L air compressor. As seen in the figure, the models were located on a 900 x 450 mm Thorlabs breadboard by using optical posts. Omega Engineering FLR 6725D with a measurement range of 1 /s to 11.8 L/s was used for primary jet flow rate measurements and Omega FLR 1002, FLR 1004, FLR 1006, and FLR 1202 covering measurement range from 0.000666 L/s to 0.3333 L/s were used to measure the control jet flow rate. The CTA system was Dantec Dynamics Mini-CTA and the probe (Dantec 55P16) provided with the system was made of plated tungsten wire (5 μm diameter and 1.2 mm long). The probe is placed at a distance away from the exit of the models on a motorized translation stage (Thorlabs MTS50M-Z8) with a travel range of 50 mm and measurements from all sensors were acquired by NI USB 6363 DAQ device. NI Labview DAQ software was used for data acquisition and simultaneous control of the motorized stage.

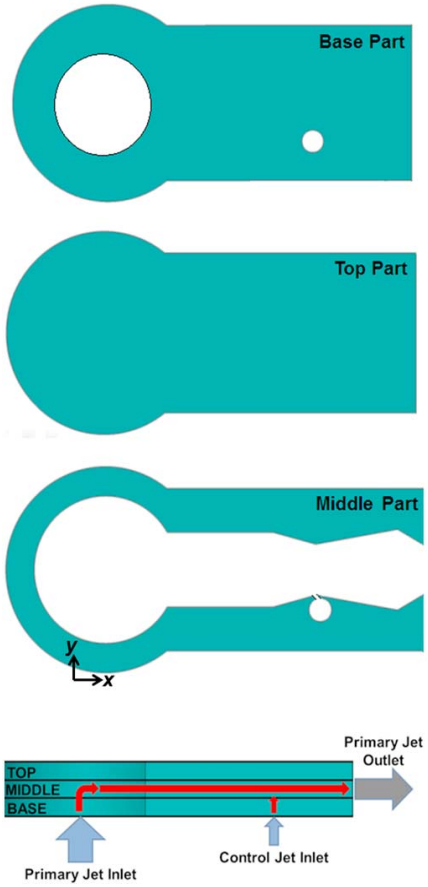

Fig. 4. Three part design and flow paths of the primary and the control jets.

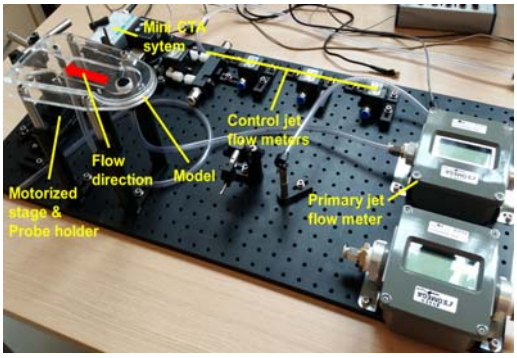

Fig. 5. Actual experimental setup.

The velocity profile for a given model under given set of conditions (primary jet flow rate, control jet flow rate etc.) was consisted of 26 measurement points (2 mm apart starting with the measurement at 0 mm) and each point's final measurement was average of 2 s of measurements at 10kHz. For some cases, higher control flow rates couldn't be measured due to the limitation of the equipment so these results are not presented and comparison was not possible.

Calibration of the CTA probe was done by using King's Law between 0 m/s to 110 m/s and between 0° to 50° with the help of a hotwire calibrator system. The uncertainty was determined as ±3% of the cited values and each measurement was corrected for temperature effects by using NI USB-TC01 thermocouple device during the calibration and the measurements. Each velocity measurement on the actual experimental models was also corrected based on the calculated vectoring angle in order to provide accurate value of the velocity since the motion of the probe was always parallel to the exit of the model regardless of the vectoring angle as shown in Fig. 6.

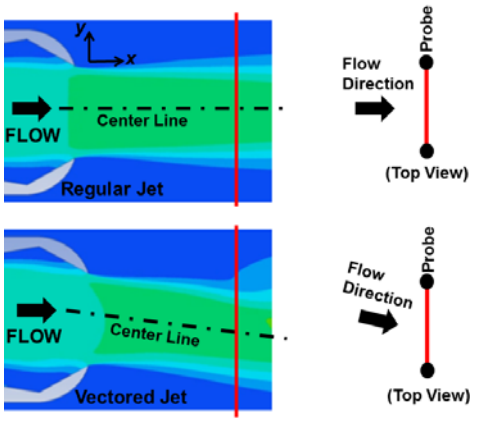

Fig. 6. Measurement path (red lines in the left image) and probe orientation for regular jet and vectored jet.

Understanding the measurement methodology of this study requires brief discussion of the different flow regions of jet flows and velocity profiles in these regions. Turbulent jets are consisted of three main distinct flow regions. First region or the initial length is the core region of the jet where the velocity is assumed to be identical to the exit velocity of the jet and the fluid is entirely made up by the jet fluid. The second is the transition region where the jet is entrained by the quiescent fluid and this entrainment reached to the centerline of the jet exit and core region is disappeared. The last region is the fully developed region and the formation of eddies are balanced by the decreasing velocities in the center region. The velocity profiles will differ depending on the region where the measurement is taken. However, when the velocity profiles are closely examined the highest velocity is always observed on the centerline of the jet (Blevins 1984). Therefore, if the maximum velocity point of a jet can be determined, the vectoring angle can be calculated based on this point.

In order to determine the vectoring angle of a model the probe should be placed after the core region since the maximum velocity in the core region occurs at more than one point. Although a survey of literature for jets issued from rectangular nozzles shows that the core region length varies from study to study and depends on Re range, the core region length was reported to be between five to seven times of the hydraulic diameter of the jet nozzle exit for the Re range considered in this study (Albertson *et al.* 1950; Van der Hegge Zijnen 1958; Schauer and Eutis 1963; Trentacoste and Sforza 1966). For this reason, the CTA probe was located eight times of the hydraulic diameter away from the nozzle exit. Although the total uncertainty in vectoring angle measurements varies based on this probe location, the highest uncertainty for thrust vectoring measurements was ±1.5°.

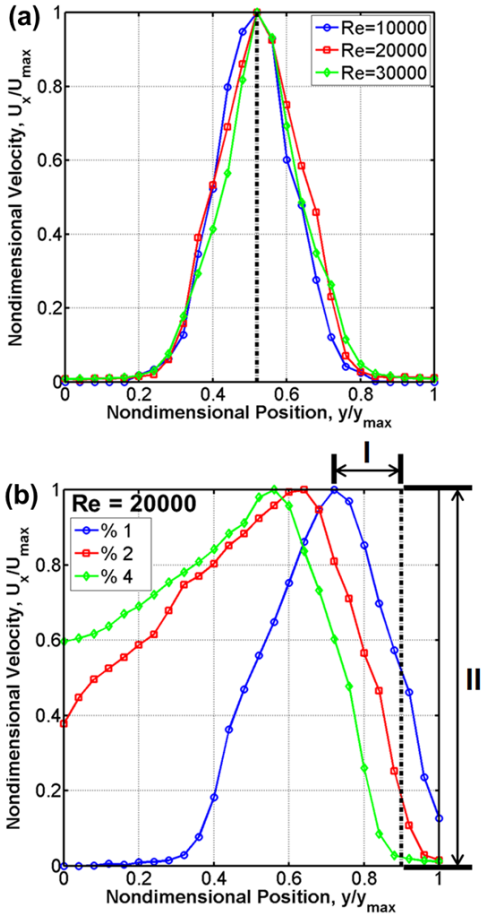

Fig. 7. No control case velocity profile (a), and controlled case velocity profiles for various control jet flow rates (b) for M3.

Figure 7 shows the velocity profiles for no control and controlled cases for Model 3 (M3) at various conditions. The dashed black line shows the geometrical centerline of the exit nozzle in both images. As expected the highest velocity for no control cases are observed on the centerline of the nozzle exit for Re range from 10000 to 30000 as

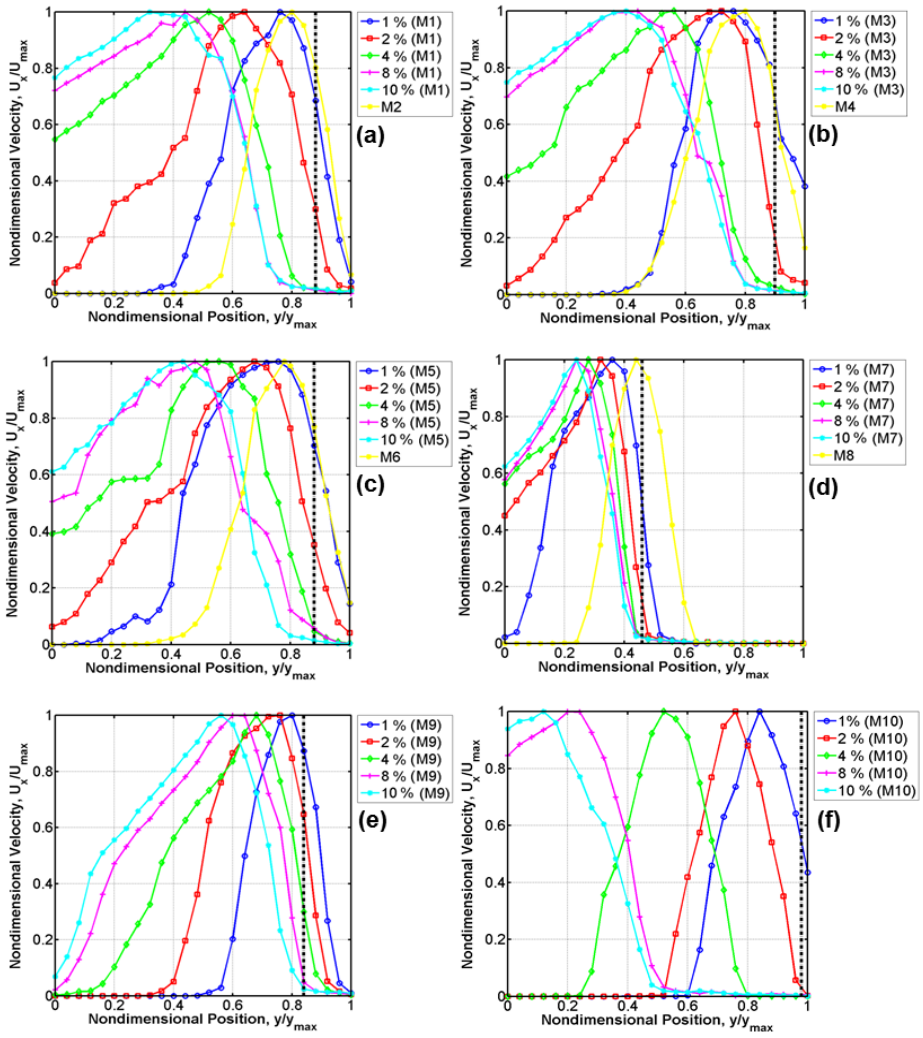

Fig. 8. Velocity profiles for all models at Re of 10000 for various control conditions.

seen in Fig. 7a. On the other hand, for Re of 20000 shown in Fig. 7b, the centerline containing the highest velocity point moved further away from the centerline of the exit nozzle as the control jet flow rate is increased.

The vector angle calculation is based on the highest velocity point deflection distance from the exit nozzle centerline depicted as I in Fig. 7b, and the vertical distance of the probe to the exit nozzle shown as II on the same figure. The tangent of I/II provides the vectoring angle. The strength of the fluidic control shown as %1, %2, and %4 in Fig. 7b is defined by the ratio of the control jet flow rate to the main jet flow rate. Nondimensional velocity in this figure was obtained by dividing the measured velocity to the maximum velocity for that primary jet flow rate and nondimensional position was obtained by dividing the probe measurement location to the motorized stage maximum displacement limit of 50 mm. Furthermore, the whole velocity profiles for the controlled cases were not fully captured due to the limitation of the maximum displacement limit of the motorized stage as seen in Fig. 7b. However, the highest velocity point was always captured in order to be able to calculate the vectoring angle.

3. RESULTS

3.1 Velocity Profiles

Obtaining velocity profiles for various flow conditions is required to assess the vectoring performance of the experimental models. In this section the velocity profiles for Re of 10000 will be presented while the vectoring angle results for Re of 20000 and 30000 will be discussed in the next section along with the vectoring angle results for Re of 10000. As mentioned before, for some cases, higher primary and control jet flow rates couldn't be measured due to the limitation of the equipment so these results are not presented and comparison was not possible.

Figures 8 (a-f) show the velocity profiles for all experimental models at Re of 10000. In these images, the dashed black line shows the geometrical centerline of the primary jet exit nozzle. Figure 8a provides the comparison between M1 and M2.

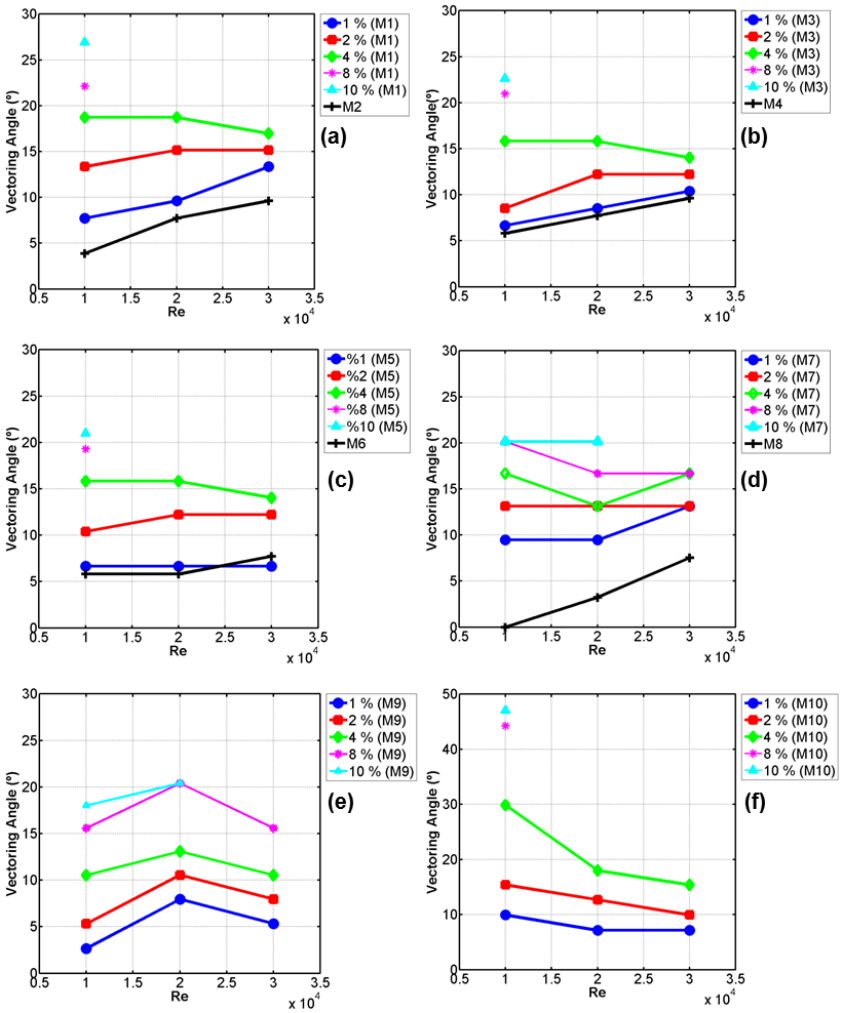

Fig. 9. Vectoring angles for all models for various control conditions at Re from 10000 to 30000.

Although flow control with M2 was able to manipulate the velocity profile, it was less effective than M1 which exhibited more and more deflection as the control jet flow rate was increased. This increase in control jet flow rate causes the main jet to be pushed more towards the wall and attach to it earlier causing increased vectoring angle. However, as M2 all the self-injection models have a constant injection channel in which the flow rate through the channel is strict function of the main jet flow conditions. Therefore, no control on injection flow rate was possible due to this fact.

The very same pattern was also observed between M3 and M4 (Fig. 8b) also between M5 and M6 (Fig. 8c). Although for M7 and M8 in Fig. 8d pattern was similar, the deflection of the velocity profile was diminished. M9 which had an enlarged region after the first throat of the model and 45° injection angle shows deflection for all tested control jet flow rates. Interestingly M10 in Fig. 8f, single throat with a small step addition model, showed a significant deflection in the velocity profiles indicating a higher vectoring angle. This deflection in the velocity profiles were used to obtain the vectoring angle for models at each flow condition considered in this study. Note that velocity profile mainly widens as the vectoring angle increases as the jet core is skewed towards vectoring direction.

3.2 Vectoring Performance Comparisons

Vectoring performance comparisons were based on the vectoring angle calculated from deflections in the velocity profiles. Fig. 9a presents the vectoring angle obtained for M1 and M2 at Re range from 10000 to 30000. As seen in the figure for M1 (up to 4%) and for M2 the vectoring angle increased with the increasing primary jet flow rate. However, for M1 the vectoring angle was constant at 4% as the primary jet flow rate was increased and then it decreased at Re of 30000. This is most likely due to the fact that the higher speed main jet flow does not have enough wall length to attach more effectively to the upper wall in the recessed cavity region as similar trend was seen for M3, M4, M5 and M6. For Re of 10000 the vectoring angle increased from 7.72° to 26.95°. On the other hand, self-injection double throat design exhibit weaker performance and the vectoring angle varied from 3.88° to 9.62°. Note that, further measurements for M1 for higher Re were not possible due to the limitation of the experimental equipment as the single points represents the results only for Re of 10000.

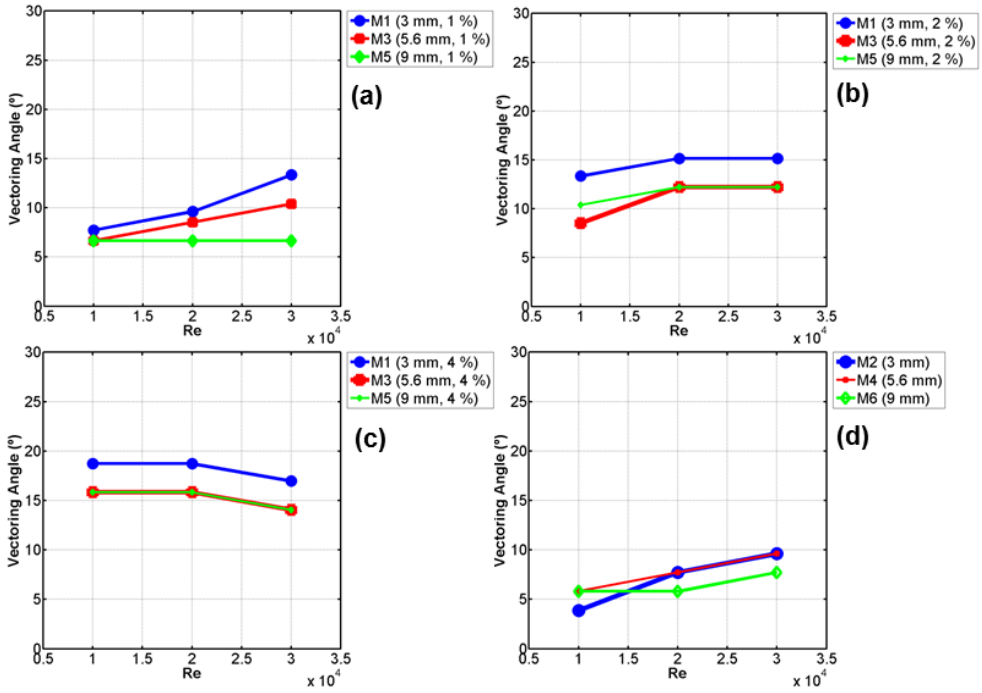

Fig. 10. Effect of the depth on the vectoring performance of models M1 to M6.

The comparison for M3 and M4 in Fig. 9b, shows a weaker performance for M4 compared to M3. While M4 has similar values compared to M2, the overall vectoring angles observed for M1 were decreased for M3. Figure 9c presents the vectoring angles for M5 and M6. Self-injection double throat M6 resulted a higher vectoring angle for Re of 30000. As the primary jet flow rate increases M5's vectoring capability tends to derogate. Figure 8d shows the results for the scaled versions of M1 and M2 except the injection angle was 30° for M7. When the results are observed closer M8 shows a continuous increase in vectoring angle at lower values than M7 while M7 performance for 1% and 4% injection shows an initial decrease with the increasing flow rate and an increase at Re of 30000.

All the models based on NASA's DTN design (models 1,3,5, and 7) generally showed higher vectoring angles than the self-injection designs (models 2,4,6, and 8). This is probably due to the fixed self-injection channel which is unable to provide enough amount of injection to achieve higher vectoring angles. M9 in Fig. 9e, shows an increase for all control jet injections but the vectoring angle drops after Re of 20000. The vectoring angle for M9 varies from 2.66° to 20.41°. The last model, M10, showed the highest vectoring angles for Re of 10000 with a maximum vectoring angle of 47° at 10% control jet injection. However, vectoring angles for 1%, 2%, and 4% drop as the primary jet flow rate is further increased.

Figures 10 (a-c) present the effect of the depth on the vectoring performance of the identical models with 3 mm, 5.6 mm, and 9 mm depths for 1%, 2%, and 4% control jet injection and Fig. 10d presents the effect of depth changes on the self-injection models. Both deeper models (M3 and M5), exhibited lower vectoring angles than M1. M3 and M5 showed

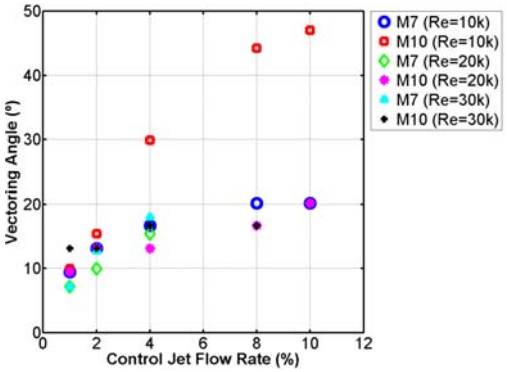

Fig. 11. Vectoring performance comparison of DTN design with single throat with a small step design.

Figure 11 presents the comparison between the DTN design (M7) and the single throat design incorporating a small step before the Coanda surface (M10). For all considered cases, M10 had higher vectoring angles and this difference was significant for Re of 10000. However, effect of vectoring was diminished for both designs as the primary jet flow rate was further increased. The success of M10 is in fact due to the small step geometry added just before the Coanda surface. Inside this step geometry a small vortex is being created which entrains the main jet towards the Coanda surface and make it attach to this Coanda surface better. similar vectoring angles with 2% and 4% control jet injections. In contrast, for 1% control jet injection the deepest model achieved the lowest vectoring angles. For self-injection models in Fig.

10d, the deeper models, M4 and M6, provided higher vectoring angles for Re of 10000. However, for Re of 30000 all models exhibited higher vectoring angles eventually.

4. CONCLUSION

In this study, vectoring performance of ten experimental models with different geometrical properties was quantified through CTA measurements. All models exhibited various vectoring angles at various flow conditions and Re. The DTN design of NASA was compared with the single throat self-injection design and it was observed that the DTN design performed higher vectoring angles for considered geometrical outlines. However, effect of the self-injection channel dimensions that dictate the self-injection jet flow rate was not quantified and this might play a key role for effectiveness of the self-injection design. The depth studies indicate that the effectiveness of the vectoring generally decreases for the DTN and self-injection designs. M9 with an enlarged region after the first throat was observed to lose its effectiveness as the Re increased. The last model with single throat and a small step provided the highest vectoring angle of 47° at Re of 10000. However, as the primary jet flow rate is increased the effectiveness of this model reduced while it still performed better than the DTN design of NASA. This loss of the last model is due to the decreasing attachment of the jet to the Coanda surface as the primary jet flow rate is increased.

ACKNOWLEDGEMENTS

This project was supported through The Scientific and Technological Research Council of Turkey (TUBITAK) 3001 Program with a project number of 114M093.

REFERENCES

Albertson, M. L., Y. B. Dai, R. A. Jensen and H. Rouse (1950). Diffusion of Submerged Jets. *ASCE Trans.* 115, 639-697.

Allen, D. and B. L. Smith (2009). Axisymemetric Coanda-assisted vectoring. *Exp. Fluids* 46, 55-64.

Benard, N., J. Jolibois, M. Forte, G. Touchard and E. Moreau (2007). Control of an axissymetric subsonic air jet by plasma actuator. *Exp. Fluids* 43, 603-616.

Berrier, B. L. and M. L. Mason (1988). Static performance of an axisymmetric nozzle with post-exit vanes for multiaxis thrust vectoring. *NASA TP-2800.*

Berrier, B. L. and J. G. Taylor (1990). Internal Performance of two nozzles utilizing gimbal concepts for thrust vectoring. *NASA TP-2991.*

Bettridge, M. W., B. L. Smith and R. E. Spall (2006). Aerodynamic jet steering using blowing and suction. *Exp. Fluids* 40, 776-785.

Blevins, R. D. (1984). *Applied Fluid Dynamics Handbook*. Van Nostrand Reinhold Co., New York.

Bougas, L. and M. Hornung (2013). Propulsion system integration and thrust vectoring aspects for scaled jet UAVs. *CEAS Aeronautical Journal* 4(3), 327-343.

Carson, G. T. and F. J. Capone (1991). Static Internal Performance an Axisymmetric Nozzle with Multiaxis Thrust Vectoring Capability. *NASA TM-4237.*

Coanda, H. (1936). Device for Deflecting a Stream of Elastic Fluid Projected into an Elastic Fluid. U.S. Patent 2,052,869, September 1.

Deere, K. A. (2000). Computational investigation of the aerodynamic effects on fluidic thrust vectoring. In *proceeding of 36th AIAA/ASME/SAE/ASEE Joint Propulsion Conference and Exhibit*, Huntsville, Alabama, AL (AIAA 2000-3598).

Deere, K. A. (2003). Summary of Fluidic Thrust Vectoring Research Conducted at NASA Langley Research Center. In *proceeding of 21st AIAA Applied Aerodynamics Conference*, Orlando, FL.

Deere, K. A., B. L. Berrier, J. D. Flamm and S. K. Johnson (2003). Computational Study of Fluidic Thrust Vectoring Using Separation Control in a Nozzle. In *proceeding of 21st AIAA Applied Aerodynamics Conference*, Orlando, FL.

Deere, K. A., B. L. Berrier, J. D. Flamm and S. K. Johnson (2005). A computational study of a new dual throat fluidic thrust vectoring nozzle concept. In *proceeding of 41st AIAA/ASME/SAE/ASEE Joint Propulsion Conference and Exhibit*, Tucson, AZ.

Dores, D., M .M. Santos, A. Krothapalli, L. Lourenco, E. Collins Jr, F. Alvi and P. Strykowski (2006). Characterization of a counterflow thrust vectoring scheme on a gas turbine engine exhaust jet. In *proceeding of 3rd AIAA Flow Control Conference*, San Francisco, CA.

Flamm, J. D. (1998). Experimental study of a nozzle using fluidic counterflow for thrust vectoring. In *proceeding of 34th AIAA/ASME/SAE/ASEE Joint Propulsion Conference and Exhibit*, Cleveland, OH.

Guo, D., A. W. Cary and R. K. Agarwal (2003). Numerical simulation of vectoring of a primary jet with a synthetic jet. *AIAA J.* 41(12), 2364-2370.

Heidari, M. r. and A. R. Pouramir (2016). Investigation and comparison effects of fluid injection type in thrust vector control. *J. Appl. Fluid Mech.* 9(1), 19-26.

Matsuno, T., M. Kawaguchi, N. Fujita, G. Yamada

and H. Kawazoe (2012). Jet vectoring and enhancement of flow control performance of trielectrode plasma actuator utilizing sliding discharge. In *proceeding of 6th AIAA Flow Control Conference*, New Orleans, LA.

Pack, L. G. and A. Seifert (2001). Periodic excitation for jet vectoring and enhanced spreading. *J. Aircraft* 38(3), 486-495.

Porter, C., A. Abbas, K. Cohen, T. McLaughlin and C. L. Enloe (2009). Spatially distributed forcing and jet vectoring with a plasma actuator. *AIAA J.* 47(6), 1368-1378.

Raman, G., S. Packiarajan, G. Papadopoulos C. Weissman and S. Raghu (2005). Jet thrust vectoring using a miniature fluidic oscillator. *Aeronaut J.* 109, 129-138.

Reba, I. (1966). Applications of the Coanda effect. *Scientific American* 214(6), 84-92.

Schauer, J. J. and R .H. Eustis (1963). The flow development and heat transfer characteristics of plane turbulent impinging jets. Tech. Rep. 3, Dept Mech Eng, Stanford Un

Smith, B. L. and A. Glezer (2002). Jet vectoring using synthetic jets. *J. Fluid Mech.* 458, 1-34.

Strykowski, P. J., A. Krothapalli and D. J. Forliti, (1996). Counterflow thrust vectoring of supersonic jets. *AIAA J.* 34(11), 2306-2314.

Trentacoste, N. and P. M. Sforza (1966). An Experimental investigation of three-dimensional free mixing in incompressible, turbulent free jets. Polytechnic institute of Brooklyn. Dept. of Aerospace Engineering and Applied Mechanic Report PlBAL-871

Van der Hegge Zijnen, B. G. (1958). Measurements of the velocity distribution in a plane turbulent jet of air. *Applied Scientific Research, Section A* 7(4), 256-276.

Wilde, P., K. Gill, S. Michie and W. Crowther (2008). Integrated design of fluidic flight controls for a flapless aircraft. *46th AIAA Aerospace Sciences Meeting and Exhibit*, Reno, NV.

Yang, J. T., C K. Chen K. J. Tsai W. Z. Lin and H. J. Sheen (2007). A novel fluidic oscillator incorporating step-shaped attachment walls. *Sensors and Actuators A: Physical* 135(2), 476-483.